JOURNAL OF GUIDANCE, CONTROL, AND DYNAMICS
Vol. 24, No. 6, November–December 2001

Fuel-Optimal, Low-Thrust, Three-Dimensional Earth–Mars Trajectories

R. S. Nah* and S. R. Vadali†
Texas A&M University, College Station, Texas 77843-3141
and
E. Braden‡
NASA Johnson Space Center, Houston, Texas 77058

Fuel-optimal three-dimensional trajectories from Earth to Mars for spacecraft powered by a low-thrust rocket with variable specific impulse capability are presented. The problem formulation treats the spacecraft mass as a state variable, thus coupling the spacecraft design to the trajectory optimization. Gravitational effects of the sun, Earth, and Mars are included throughout an entire trajectory. To avoid numerical sensitivity, the trajectory is divided into segments, each defined with respect to a different central body. These segments are patched at intermediate time points, with proper matching conditions on the states and costates. The optimization problem is solved using an indirect multiple shooting method. Details of trajectories for the outbound legs of crewed missions to Mars, with trip times of 145 and 168 days, are shown. Effects due to variations in the trip time, departure and arrival orbit inclinations, initial fuel mass, and power level are investigated.

Introduction

EVER since the success of lunar missions, explorations to reach beyond the Earth–moon system and eventually to sustain habitats on other planets have been inspiring the development of space technologies and the astronomical sciences. Low-thrust propulsion is one of the promising technologies being extensively studied to enhance our capability for interplanetary travel. The NASA Solar Electron Propulsion Technology Application Readiness ion thruster on the Deep Space 1 mission launched by NASA in October 1998 demonstrated this concept in practice. Low-thrust electric propulsion is more efficient compared to a conventional chemical rocket. The improved efficiency does come at the expense of increased mission time. Nevertheless, a compromise between the mission duration and payload can be accomplished by modulating the thrust magnitude and direction.

Chang-Diaz et al.[1] present an experimental plasma thruster being developed at NASA Johnson Space Center. The thruster is constructed using compact, high-field, and lightweight superconductors. It uses the characteristics of an rf heating of a neutral gas like hydrogen to generate plasma and an electromagnetic field to vector the exhaust. The device is projected to be capable of specific impulse I_{sp} variations within the range of 1000–35,000 s at a rated power of 10 MW. The specific mass and efficiency of the power plant are estimated to be approximately 6 kg/kW and 60%, respectively.

Melbourne[2] documented numerous analyses on interplanetary missions based on an unconventional low-thrust propulsion system. In his formulation, the mission payload design and trajectory optimization are uncoupled, that is, the fuel requirement is computed after optimization. These studies focus on heliocentric transfers between the spheres of influence of the departure and target planets. Spiral escapes and captures are simply approximated by assuming tangential thrusting. By use of a similar approach, Chang-Diaz et al.[1] have assessed the capabilities of the low-thrust variable I_{sp} plasma thruster and the feasibility of a trip to Mars. To a greater extent, Sheppard et al.[3] have conducted mission analyses for crewed and uncrewed Mars missions based on the same power-limited propulsion system and by following Melbourne's[2] approach as well. Kechichian[4] presents an overview of the literature on optimal low-thrust orbit transfer problems by utilizing equinoctial orbital elements as the states. A penalty function approach is used to solve the orbit transfer problem with variable, bounded I_{sp}.

Demonstrations of various numerical techniques for solving low-thrust optimization problems can also be found in the literature. Kluever[5] presents a variety of analyses using a direct shooting method based on sequential quadratic programming. Coverstone-Carroll and Williams[6] demonstrate the use of differential inclusions to determine optimal low-thrust interplanetary trajectories. Enright and Conway[7] present two variants of the direct transcription techniques, the collocation and parallel shooting methods, for finite thrust spacecraft trajectory optimization. Scheel and Conway[8] present a discretized version of the parallel shooting method to solve minimum-time problems for low Earth orbit (LEO) to geosynchronous orbit (GEO) and GEO to outer orbit transfers.

The following references treat interplanetary trajectory optimizations by including the gravitational effects of multiple bodies. Pierson and Kluever[9] and Kluever and Pierson[10] present fuel-optimal lunar trajectories computed by using a combination of direct and indirect approaches. In these works, a sequence of thrusting and coasting arcs is assumed. Solutions to three separate subproblems, an Earth-escape spiral, a translunar coast arc, and a lunar capture spiral, are used to initiate the search process for the optimal lunar trajectory. Application of collocation and nonlinear programming to the solution of minimum-time/fuel Earth–Mars trajectories is presented by Tang and Conway.[11] In their work, a patch-conic equivalent approximation is used, and thrust acceleration is treated as a constant. Vadali et al.[12] present fuel-optimal planar Earth–Mars trajectories with the implementation of the propulsion characteristics of the plasma thruster documented in Ref. 1. The numerical solutions obtained using a multiple-shooting method demonstrate the nature of the optimal thrust modulations and the improvements in the fuel usage over current estimates.

This paper addresses the extension of work presented in Ref. 12. It deals with the computations of fuel-optimal, three-dimensional trajectories from a circular Earth parking orbit to a circular arrival orbit about Mars within a specified time frame, for a vehicle with the aforementioned plasma propulsion capability. The trajectories determined in this work simulate outbound legs of crewed missions to Mars, launched in the year 2014. To accommodate the limits on the I_{sp}, the payload design is coupled to the trajectory optimization by treating the spacecraft mass as a state variable. Unlike the

Received 21 April 2000; revision received 23 February 2001; accepted for publication 26 March 2001.

*Graduate Student, Department of Aerospace Engineering.
†Professor, Department of Aerospace Engineering; svadali@aero.tamu.edu. Associate Fellow AIAA.
‡Aerospace Engineer, EG5/Advanced Mission Design.

planar optimization problems considered in Ref. 12, the effects due to inclinations and eccentricities of the planetary orbits of Earth and Mars are taken into account in the three-dimensional trajectory computations. The planetary states corresponding to a specific departure date were obtained from the ephemerides and then propagated along with the spacecraft trajectory using two-body mechanics. The departure date for all of the trajectories considered in this paper is 1 February 2014, selected based on the results of Ref. 12. The radius of the Earth parking orbit is 1200 km and that of the areosynchronous orbit is equal to six Mars radii. The departure and arrival parking orbit inclinations are specified. For the purpose of analysis, trajectories were obtained with trip times ranging from 142 to 168 days, initial spacecraft masses from 420,000 to 525,000 kg, and power levels from 10 MW to as low as 9.3 MW.

The optimization problems were solved using an indirect multiple-shooting method. The technique employs Newton's method with line searches and backtracking to seek and locate a local extremum. In spite of the sensitivity inherent in the method, the indirect approach provides highly accurate solutions and an assurance of optimality. Because of the complexity involved, a number of subproblems dealing with relaxed boundary conditions were solved a priori, before attempting to solve for a complete Earth–Mars trajectory. Following the approach utilized in Refs. 9, 10, and 12, simpler problems that cover only single phases were first solved and then linked to initiate the search for the more complex optimal trajectories. The solution to the complete problem satisfies all of the necessary conditions of optimality to numerical accuracy.

System Equations

Three sets of coordinate systems have been utilized to determine the trajectories: a geocentric spherical rotating coordinate system, a heliocentric rectangular inertial frame, and an areocentric spherical rotating frame. The heliocentric inertial frame is shown in Fig. 1, with the $\{\hat{\underline{x}}, \hat{\underline{y}}, \hat{\underline{z}}\}$ unit vectors. The x axis points in the direction of the vernal equinox, the z axis is perpendicular to the ecliptic plane, and the y axis is in the direction perpendicular to the x–z plane. A planetocentric coordinate system (either geocentric or areocentric) is shown in Fig. 2 with the $\{\hat{\underline{e}}_{r_1}, \hat{\underline{e}}_{\theta_1}, \hat{\underline{e}}_{\phi_1}\}$ unit vectors. In Fig. 2, planet p represents the planet at the origin of the planetocentric coordinate system of interest and planet q simply denotes the other planet orbiting the sun. In the geocentric frame, p and q refer to the Earth and Mars, respectively, whereas in the areocentric frame, the reverse applies. Note that the inertial frame $\{\hat{\underline{x}}', \hat{\underline{y}}', \hat{\underline{z}}'\}$ in Fig. 2 is aligned with the orbital plane of planet p, with $\hat{\underline{z}}'$ perpendicular to the plane. Ω_p and i_p are, respectively, the right ascension and inclination of the planet's orbit about the sun.

Trajectory Dynamics Relative to the Heliocentric Frame

The equations of motion with respect to the heliocentric rectangular inertial coordinate system were used in the computation of the heliocentric transfer arc. It is emphasized, however, that the heliocentric transfer arc can also be generated using the planetocentric equations of motion, which will be presented later. It was found during the course of this work that computations using only the planetocentric dynamics have better convergence properties. The heliocentric-referenced equations, therefore, were only utilized in the early stages of the computational procedure. The heliocentric equations are

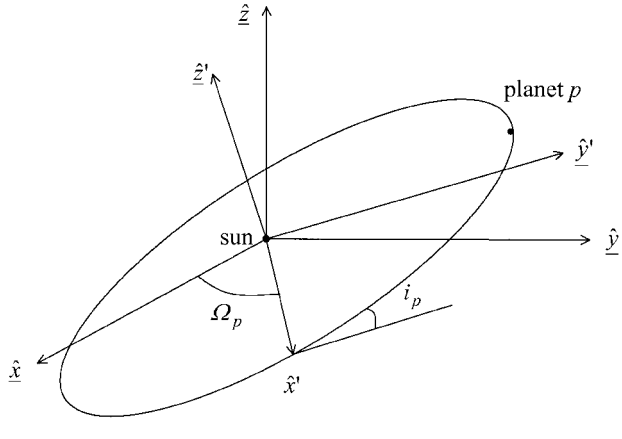

Fig. 1 Heliocentric inertial coordinate systems.

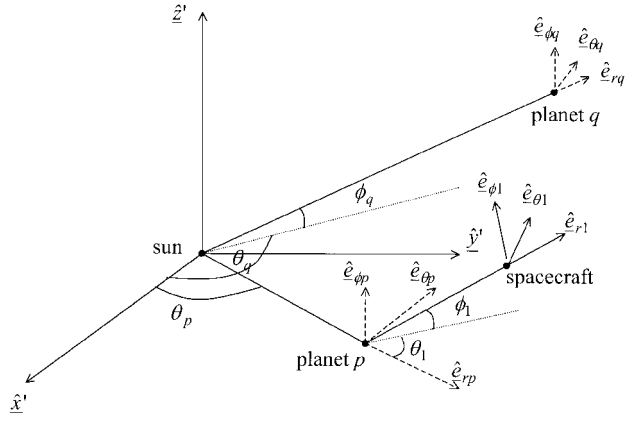

Fig. 2 Heliocentric and planetocentric spherical coordinate systems.

$$\dot{x} = V_x \tag{1}$$

$$\dot{y} = V_y \tag{2}$$

$$\dot{z} = V_z \tag{3}$$

$$\dot{V}_x = -\frac{\mu_S}{r^3}x - \frac{\mu_E}{|\boldsymbol{r}-\boldsymbol{R}_E|^3}(x-x_E) - \frac{\mu_M}{|\boldsymbol{r}-\boldsymbol{R}_M|^3}(x-x_M) + \frac{2\varepsilon P}{mg}u_x \tag{4}$$

$$\dot{V}_y = -\frac{\mu_S}{r^3}y - \frac{\mu_E}{|\boldsymbol{r}-\boldsymbol{R}_E|^3}(y-y_E) - \frac{\mu_M}{|\boldsymbol{r}-\boldsymbol{R}_M|^3}(y-y_M) + \frac{2\varepsilon P}{mg}u_y \tag{5}$$

$$\dot{V}_z = -\frac{\mu_S}{r^3}z - \frac{\mu_E}{|\boldsymbol{r}-\boldsymbol{R}_E|^3}(z-z_E) - \frac{\mu_M}{|\boldsymbol{r}-\boldsymbol{R}_M|^3}(z-z_M) + \frac{2\varepsilon P}{mg}u_z \tag{6}$$

$$\dot{m} = -(2\varepsilon P/g^2)\left(u_x^2 + u_y^2 + u_z^2\right) \tag{7}$$

where

$$r = \sqrt{x^2 + y^2 + z^2} \tag{8}$$

$$|\boldsymbol{r}-\boldsymbol{R}_E| = \sqrt{(x-x_E)^2 + (y-y_E)^2 + (z-z_E)^2} \tag{9}$$

$$|\boldsymbol{r}-\boldsymbol{R}_M| = \sqrt{(x-x_M)^2 + (y-y_M)^2 + (z-z_M)^2} \tag{10}$$

In the preceding equations, x, y, and z, are the three position components of the spacecraft relative to the sun. V_x, V_y, and V_z, are the three inertial velocity components of the spacecraft; m is the spacecraft mass; and vectors $\boldsymbol{r}$, $\boldsymbol{R}_E$, and $\boldsymbol{R}_M$ represent positions of the spacecraft, Earth, and Mars with respect to the sun, respectively. The position components of the Earth relative to the sun are given by x_E, y_E, and z_E. The position of Mars is given by x_M, y_M, and z_M. The constants μ_S, μ_E, and μ_M are the gravitational parameters of the sun, Earth, and Mars, respectively. P is the power level, ε is the power plant efficiency, and g is the gravitational acceleration at sea level on Earth. The control variables u_x, u_y, and u_z are related to I_{sp} and the two thrust angles, α and β by

$$\begin{Bmatrix} u_x \\ u_y \\ u_z \end{Bmatrix} = \frac{1}{I_{\text{sp}}} \begin{Bmatrix} \sin\alpha\cos\beta \\ \cos\alpha\cos\beta \\ \sin\beta \end{Bmatrix} \tag{11}$$

The in-plane thrust steering angle α is measured from the y axis to the projection of the thrust vector on the x–y plane, and the out-of-plane angle β is measured from the x–y plane to the thrust vector.

Trajectory Dynamics Relative to the Geocentric and Areocentric Frames

The state equations with respect to the geocentric spherical coordinate system were used to describe the Earth-escape spiral:

$$\dot{r}_1 = V_{r_1} \tag{12}$$

$$\dot{\theta}_1 = V_{\theta_1}/r_1 \cos\phi_1 \tag{13}$$

$$\dot{\phi}_1 = V_{\phi_1}/r_1 \tag{14}$$

$$\begin{aligned}\dot{V}_{r_1} = {} & V_{\theta_1}^2/r_1 + V_{\phi_1}^2/r_1 + 2\dot{\theta}_E V_{\theta_1}\cos\phi_1 + \dot{\theta}_E^2\big(r_1\cos^2\phi_1 \\ & + R_E\cos\theta_1\cos\phi_1\big) - \ddot{R}_E\cos\theta_1\cos\phi_1 - 2\dot{R}_E\dot{\theta}_E\sin\theta_1\cos\phi_1 \\ & - R_E\ddot{\theta}_E\sin\theta_1\cos\phi_1 - \mu_E/r_1^2 - \mu_S(r_1 + R_E\cos\theta_1\cos\phi_1)/r_S^3 \\ & - \mu_M\{r_1 + R_E\cos\theta_1\cos\phi_1 - R_M[\cos\phi_M\cos(\theta_1 + \theta_E \\ & - \theta_M)\cos\phi_1 + \sin\phi_M\sin\phi_1]\}/r_2^3 + (2\varepsilon P/m_1 g)u_{r_1}\end{aligned} \tag{15}$$

$$\begin{aligned}\dot{V}_{\theta_1} = {} & -V_{r_1}V_{\theta_1}/r_1 + V_{\theta_1}V_{\phi_1}\sin\phi_1/r_1\cos\phi_1 - 2\dot{\theta}_E\big(V_{r_1}\cos\phi_1 \\ & - V_{\phi_1}\sin\phi_1\big) - R_E\dot{\theta}_E^2\sin\theta_1 + \ddot{R}_E\sin\theta_1 - 2\dot{R}_E\dot{\theta}_E\cos\theta_1 \\ & - \ddot{\theta}_E(r_1\cos\phi_1 + R_E\cos\theta_1) + \mu_S R_E\sin\theta_1/r_S^3 + \mu_M[R_E\sin\theta_1 \\ & - R_M\cos\phi_M\sin(\theta_1 + \theta_E - \theta_M)]/r_2^3 + (2\varepsilon P/m_1 g)u_{\theta 1}\end{aligned} \tag{16}$$

$$\begin{aligned}\dot{V}_{\phi_1} = {} & -V_{r_1}V_{\phi_1}/r_1 - V_{\theta_1}^2\sin\phi_1/r_1\cos\phi_1 - 2\dot{\theta}_E V_{\theta_1}\sin\phi_1 \\ & - \dot{\theta}_E^2(r_1\sin\phi_1\cos\phi_1 + R_E\cos\theta_1\sin\phi_1) + \ddot{R}_E\cos\theta_1\sin\phi_1 \\ & + 2\dot{R}_E\dot{\theta}_E\sin\theta_1\sin\phi_1 + R_E\ddot{\theta}_E\sin\theta_1\sin\phi_1 \\ & + \mu_S R_E\cos\theta_1\sin\phi_1/r_S^3 + \mu_M\{R_E\cos\theta_1\sin\phi_1 \\ & - R_M[\cos\phi_M\cos(\theta_1 + \theta_E - \theta_M)\sin\phi_1 \\ & - \sin\phi_M\cos\phi_1]\}/r_2^3 + (2\varepsilon P/m_1 g)u_{\phi_1}\end{aligned} \tag{17}$$

$$\dot{m}_1 = -(2\varepsilon P/g^2)\big(u_{r_1}^2 + u_{\theta_1}^2 + u_{\phi_1}^2\big) \tag{18}$$

in which

$$r_S = \sqrt{r_1^2 + R_E^2 + 2R_E r_1\cos\theta_1\cos\phi_1} \tag{19}$$

$$\begin{aligned}r_2 = {} & \big\{r_1^2 + R_E^2 + R_M^2 + 2R_E r_1\cos\theta_1\cos\phi_1 \\ & - 2R_M r_1[\cos\phi_M\cos(\theta_1 + \theta_E - \theta_M)\cos\phi_1 + \sin\phi_M\sin\phi_1] \\ & - 2R_E R_M\cos\theta_M\cos(\theta_M - \theta_E)\big\}^{\frac{1}{2}}\end{aligned} \tag{20}$$

where r_1 is the distance of the spacecraft from the Earth; V_{r_1}, V_{θ_1}, and V_{ϕ_1} are the noninertial velocity components in the radial, tangential, and out-of-plane directions, respectively; m_1 is the spacecraft mass; r_S and r_2 are the distances of the spacecraft from the sun and Mars, respectively; and R_E and R_M are the distances of the Earth and Mars with respect to the sun. All of the angular variables are defined as shown in Fig. 2, after replacing subscripts p and q with E and M, respectively. The control variables u_{r_1}, u_{θ_1}, and u_{ϕ_1} are associated with the thrust in the radial, tangential, and out-of-plane directions, respectively, as

$$\begin{Bmatrix} u_{r_1} \\ u_{\theta_1} \\ u_{\phi_1} \end{Bmatrix} = \frac{1}{I_{\text{sp}}}\begin{Bmatrix} \sin\alpha_1\cos\beta_1 \\ \cos\alpha_1\cos\beta_1 \\ \sin\beta_1 \end{Bmatrix} \tag{21}$$

where α_1 is the thrust angle measured from the e_{θ_1} axis to the projection of the thrust vector on the e_{r_1}–e_{θ_1} plane, and β_1 is the angle measured perpendicularly from e_{r_1}–e_{θ_1} plane to the thrust vector.

Equations (12–21) describe the trajectory dynamics with respect to the areocentric spherical coordinate system as well, if subscripts E and M are interchanged. These equations were utilized for the computation of the Mars-capture spiral.

Optimal Control Problem

This section deals with the formulation of the optimal control problem and the necessary conditions of optimality.

Performance Index

The objective of this work is to minimize the fuel expended in delivering the spacecraft from a circular Earth parking orbit to a circular orbit about Mars. With the trip time fixed and the initial fuel mass specified, the objective is equivalent to maximizing the spacecraft mass at insertion into the Mars parking orbit. Hence, the performance index is

$$J = -m_1(t_f) \tag{22}$$

Dynamic Constraints

The entire Earth–Mars trajectory can be treated as having three segments: the Earth-escape spiral, the heliocentric transfer arc, and the Mars-capture spiral. The geocentric segment, from t_0 to an intermediate time t_1, is modeled by Eqs. (12–18). Equations (1–7) model the heliocentric segment, from t_1 to another intermediate time t_2. The areocentric segment, from t_2 to t_f, is described by Eqs. (12–18), with subscripts E and M interchanged. Corresponding to each segment, costate equations resulting from the necessary conditions were integrated along with the state equations to compute the optimal controls. Because of the complexity of the equations and limitation of space, the costate equations are not presented in this paper. They can, however, be obtained from Ref. 13.

Boundary Constraints

The boundary constraints are the initial and final conditions that specify the departure and arrival orbits, respectively, and the transversality conditions at the various terminal points.

The initial conditions specified with respect to the geocentric frame at t_0 for a departure orbit in the Earth's orbital plane, that is, the x'–y' plane, are

$$\Psi_{0_1} = r_1(t_0) - r_0 = 0 \tag{23}$$

$$\Psi_{0_2} = \phi_1(t_0) = 0 \tag{24}$$

$$\Psi_{0_3} = V_{r_1}(t_0) = 0 \tag{25}$$

$$\Psi_{0_4} = V_{\theta_1}(t_0) + r_0\dot{\theta}_E(t_0) - \sqrt{\mu_E/r_0} = 0 \tag{26}$$

$$\Psi_{0_5} = V_{\phi_1}(t_0) = 0 \tag{27}$$

$$\Psi_{0_6} = m_1(t_0) - m_0 = 0 \tag{28}$$

where r_0 and m_0 are known constants. Note that a direct orbit has been specified and the initial longitude $\theta_1(t_0)$ is unspecified. Associated with this set of constraints, the transversality condition[13,14] on the costate ($\boldsymbol{\lambda}$ is the costate vector) for θ_1 is

$$\lambda_{\theta_1}(t_0) = 0 \tag{29}$$

To define a departure orbit at a nonzero inclination i_0 relative to the orbital plane of Earth, the initial conditions are modified to be

$$\Psi_{0_1} = r_1(t_0) - r_0 = 0 \tag{30}$$

$$\Psi_{0_2} = V_{r_1}(t_0) = 0 \tag{31}$$

$$\Psi_{0_3} = \big[V_{\theta_1}(t_0) + r_0\dot{\theta}_E(t_0)\cos\phi_1(t_0)\big]^2 + V_{\phi_1}^2(t_0) - \mu_E/r_0 = 0 \tag{32}$$

$$\begin{aligned}\Psi_{0_4} = {} & \big[V_{\theta_1}(t_0) + r_0\dot{\theta}_E(t_0)\cos\phi_1(t_0)\big]\cos\phi_1(t_0) \\ & - \sqrt{(\mu_E/r_0)}\cos i_0 = 0\end{aligned} \tag{33}$$

$$\Psi_{0_5} = m_1(t_0) - m_0 = 0 \tag{34}$$

where i_0 can be between 0 and 180 deg, excluding 0, 90, and 180 deg. The corresponding transversality conditions[13,14] are

$$\lambda_{\theta_1}(t_0) = 0 \tag{35}$$

$$-2\nu_{0_3} r_0 \dot{\theta}_E(t_0) \sin\phi_1(t_0)\left[V_{\theta_1}(t_0) + r_0\dot{\theta}_E(t_0)\cos\phi_1(t_0)\right] - \nu_{0_4}\sin\phi_1(t_0)\left[V_{\theta_1}(t_0) + 2r_0\dot{\theta}_E(t_0)\cos\phi_1(t_0)\right] + \lambda_{\phi_1}(t_0) = 0 \tag{36}$$

$$2\nu_{0_3}\left[V_{\theta_1}(t_0) + r_0\dot{\theta}_E(t_0)\cos\phi_1(t_0)\right] + \nu_{0_4}\cos\phi_1(t_0) + \lambda_{V_{\theta_1}}(t_0) \tag{37}$$

$$2\nu_{0_3} V_{\phi_1}(t_0) + \lambda_{V_{\phi_1}}(t_0) = 0 \tag{38}$$

where ν_{0_3} and ν_{0_4} are the Lagrange multipliers associated with Ψ_{0_3} and Ψ_{0_4}, respectively.

Similar transversality conditions can be imposed at t_f with respect to the areocentric frame to specify the arrival inclination and account for terminal boundary conditions.

Intermediate Point Constraints

To ensure the continuity of the trajectory, intermediate state constraints are enforced at t_1 and t_2. Associated with these constraints are the costate jump conditions[12,13]:

$$\boldsymbol{\lambda}\left(t_1^+\right) + \left[\Psi_{1x^+}^T\right]\Big|_{t_1}\left[\Psi_{1x^-}^{-T}\right]\Big|_{t_1}\boldsymbol{\lambda}\left(t_1^-\right) = 0 \tag{39}$$

$$\boldsymbol{\lambda}\left(t_2^+\right) + \left[\Psi_{2x^+}^T\right]\Big|_{t_2}\left[\Psi_{2x^-}^{-T}\right]\Big|_{t_2}\boldsymbol{\lambda}\left(t_2^-\right) = 0 \tag{40}$$

where subscripts x^- and x^+ represent partial derivatives with respect to $\boldsymbol{x}(t_i^-)$ and $\boldsymbol{x}(t_i^+)$, respectively. They were derived based on coordinate transformation between the $\{\hat{\underline{x}}, \hat{\underline{y}}, \hat{\underline{z}}\}$ axes shown in Fig. 1 and the $\{\hat{\underline{e}}_{r_1}, \hat{\underline{e}}_{\theta_1}, \hat{\underline{e}}_{\phi_1}\}$ axes of Fig. 2. The constraints in their explicit forms can be found in Ref. 13.

Optimal Control

Besides the constraints described, the limits on the I_{sp} are enforced via a control-variable inequality constraint:

$$I_{sp_{min}} \le I_{sp} \le I_{sp_{max}} \tag{41}$$

With reference to the definition of the control vector, the preceding inequality can also be written as follows:

$$1/I_{sp_{max}} \le \sqrt{\boldsymbol{u}^T\boldsymbol{u}} \le 1/I_{sp_{min}} \tag{42}$$

According to Pontryagin's minimum principle,[14] the optimal control minimizes the Hamiltonian subject to the constraints. To apply Pontryagin's minimum principle, the part of the Hamiltonian that depends on the control variables explicitly is isolated:

$$H' = (2\varepsilon P/gm)\boldsymbol{\lambda}_V^T\boldsymbol{u} - \left(2\varepsilon P\lambda_m/g^2\right)\boldsymbol{u}^T\boldsymbol{u} \tag{43}$$

where $\boldsymbol{\lambda}_V$ is the velocity costate vector and λ_m is the mass costate. Note that m is to be replaced by m_1 in the planetocentric phases. The unconstrained optimal control obtained via the first-order necessary condition, $\partial H/\partial\boldsymbol{u} = 0$, is then given by

$$\boldsymbol{u} = (g/2m\lambda_m)\boldsymbol{\lambda}_V \tag{44}$$

To ensure a minimum, the convexity condition requires that

$$\lambda_m < 0 \tag{45}$$

As a result, Eq. (44) defines the optimal control if Eqs. (42) and (45) are not violated.

Three other conditions have to be considered. They are situations where the optimal I_{sp} is on the upper or lower limits with either $\lambda_m < 0$ or $\lambda_m > 0$. For $\lambda_m < 0$, on the lower and upper boundaries of the I_{sp} constraint, respectively, the optimal control is given by

$$\boldsymbol{u} = -\boldsymbol{\lambda}_V \Big/ I_{sp_{min}}\sqrt{\boldsymbol{\lambda}_V^T\boldsymbol{\lambda}_V} \tag{46}$$

$$\boldsymbol{u} = -\boldsymbol{\lambda}_V \Big/ I_{sp_{max}}\sqrt{\boldsymbol{\lambda}_V^T\boldsymbol{\lambda}_V} \tag{47}$$

For situations where $\lambda_m > 0$, H' is minimized if $\sqrt{(\boldsymbol{u}^T\boldsymbol{u})} = 1/I_{sp_{min}}$ and $\boldsymbol{u}$ carries the sign opposite to that of $\boldsymbol{\lambda}_V$. The solution for this condition is, therefore, the same as that given in Eq. (46). Singular arcs have not been considered in this work.

Spacecraft and Trajectory Parameters

The parameters and specifications used in this work were taken from Refs. 1 and 3. The estimated power level P is 10 MW and the power plant efficiency ε is 0.6. The lower and upper bounds of the I_{sp}, $I_{sp_{min}}$, and $I_{sp_{max}}$ are, respectively, 1000 and 35,000 s. Because the specific mass of the powerplant is assumed to be 6 kg/kW, the mass of the 10-MW power plant is 60,000 kg. Considering an estimated payload mass of 35,000 kg, the dry spacecraft mass is approximately 95,000 kg. This value serves as the limit on the final mass that determines if a particular trajectory is feasible or not. In other words, a trajectory is deemed infeasible if the resulting final mass falls below the limit. Most of the trajectories presented in this paper were determined with an initial mass of 525,000 kg, a value obtained from Ref. 3. This value of the initial mass was estimated based on an Earth–Mars transfer that is composed of a fuel-optimal heliocentric transfer arc and constant thrust Earth-escape and Mars-capture spirals with an I_{sp} of 1000 s.

At departure, the parking orbit is specified to be circular, with an altitude of 1200 km. The departure orbit inclination i_0 is specified in the range of 0–30 deg relative to the orbital plane of the Earth. At arrival, the spacecraft is required to establish a parking orbit of approximately six Mars radii (6 DU_M). The range of arrival orbit inclinations, considered relative to the orbital plane of Mars, is from 0 deg to near polar (88 deg). The fixed trip times of the trajectories determined are in the range of 142–168 days.

Method of Solution

The solution to the optimal control problem posed was obtained by treating the terminal constraints, transversality conditions, and costate jump conditions as nonlinear algebraic functions of the unknown parameters. These functions were evaluated on generation of a trajectory by applying the state, costate, and control equations with a set of guessed values for the unknowns. The system of nonlinear functions was solved using a modified Newton's method with line searches and backtracking. The tolerance of the constraint violation was set to be 10^{-10} as the convergence criterion. The differential equations were integrated using a Runge–Kutta–Fehlberg Seventh-order scheme with an accuracy of 10 digits. To avoid numerical sensitivity and to accommodate the different reference frames, appropriate canonical units for each phase of the trajectory were utilized.[15]

The subproblems that were solved to generate a complete baseline Earth–Mars trajectory are described here:

1) A 35-day maximum-energy Earth-escape trajectory was determined by using the cost function

$$J = -\left\{\left[V_{r_1}^2(t_f) + V_{\theta_1}^2(t_f) + V_{\phi 1}^2(t_f)\right]/2 - \mu_E/r_1(t_f)\right\}$$

The departure date selected was 1 February 2014. The Earth parking orbit inclination was set at 0 deg. The initial longitude $\theta_1(t_0)$ was left free. The escape asymptote with respect to Earth was set along the sun–Earth line, that is, $\theta_1(t_0) = 0$ deg. The geocentric dynamics model was utilized to solve this subproblem.

2) Next, a 110-day (from day 35 to day 145) minimum-fuel heliocentric transfer arc was determined for a subproblem. In this subproblem, the initial time, position, and velocity for the heliocentric injection were obtained from the respective final conditions for the Earth-escape trajectory obtained in step 1. The initial spacecraft mass was chosen to be 50% of the mass at Earth departure, based on the solution of the planar problem.[12] The final position and velocity of the spacecraft were specified to be close but slightly different from those of Mars. The cost function for this subproblem

was $J = -m(t_f)$. This subproblem was solved with respect to the heliocentric rectangular inertial frame.

3) A 145-day minimum-fuel trajectory from an Earth parking orbit to the proximity of Mars was determined. The same cost function as in step 2 was used. The Earth-escape and heliocentric transfer segments were patched together using the solutions obtained in steps 1 and 2. The starting conditions of step 1 and ending conditions of step 2 were used, and all of the necessary conditions as well as the intermediate point conditions were enforced.

4) A 145-day minimum-fuel trajectory, similar to that obtained in step 3, was determined, with an enforced circularization at a radius of about 600 DU_M at the final time. The circularization occurs in the plane of $i_f = 0$ deg. Only the geocentric and heliocentric dynamics were utilized. However, the final conditions were enforced with respect to the areocentric coordinate system.

5) The circularization radius was incrementally reduced to the desired value to generate a complete Earth–Mars trajectory. Only the geocentric and areocentric dynamics were used for this series of attempts. The geocentric segment covered the Earth-escape phase and most of the heliocentric transfer arc whereas the areocentric segment contained the remaining portion of the heliocentric transfer arc and the Mars-capture spiral. It was found that convergence was better with t_1 set at approximately 132 days and when the heliocentric-referenced equations were bypassed. The reduction of the final radius from 600 DU_M to 6 DU_M involved the solutions to nearly 100 subproblems. The baseline solution to the complete Earth–Mars trajectory was used to generate trajectories with various trip times as well as for other departure and arrival inclinations.

Results

Example Set 1

The solution to the 145-day fuel-optimal trajectory from a 1200 km parking orbit with $i_0 = 0$ deg to a 1-SOL orbit about Mars, with $i_f = 0$ deg, is presented first. The trajectory was obtained with an initial mass of 525,000 kg and power level of 10 MW. The Earth-escape segment for the first 30 days is presented in Fig. 3a. The in-plane and out-of-plane projections of the Mars-capture trajectory, for the final nine days, are presented in Figs. 3b and 3c, respectively. The in-plane projection shows that the spacecraft makes a sharp turn prior to circularization whereas the out-of-plane projection reveals a slight plane change near the end. The specific energy of the spacecraft relative to Earth for the 30-day escape phase is shown in Fig. 3d. It can be concluded from Fig. 3d that the spacecraft escapes the Earth's gravitational field after approximately 24 days, when parabolic speed is achieved. Numerical data reveal that the spacecraft makes 102 revolutions about the Earth before escaping. The energy relative to Mars for the 9-day capture phase is plotted in Fig. 3e. The plot shows that the capture phase begins around 140 days from departure. Note from the in-plane projection that less than a turn is made by the spacecraft to circularize its orbit about Mars. The I_{sp} variation with respect to time is shown in Fig. 3f. The I_{sp} plot shows an initial segment of maximum thrust, followed by modulations of the exhaust during the rest of the trajectory. The

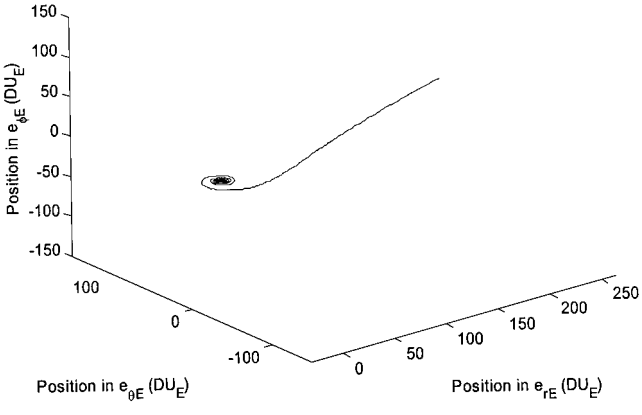

Fig. 3a Shown in geocentric frame. 30-day escape phase of 145-day trajectory.

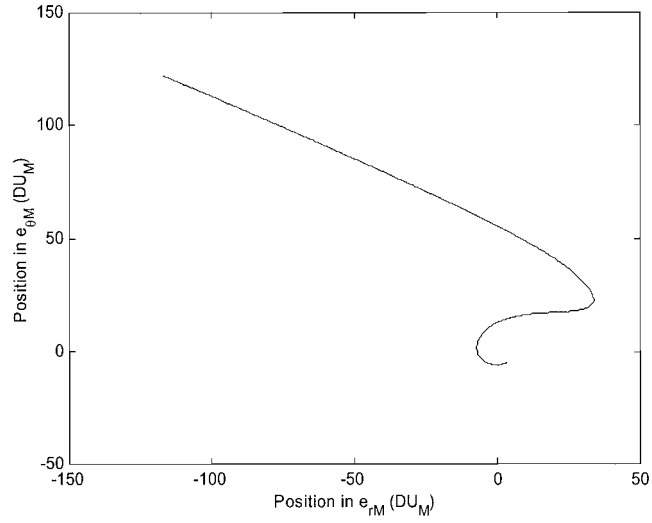

Fig. 3b In-plane projection of 9-day Mars-capture segment of 145-day trajectory.

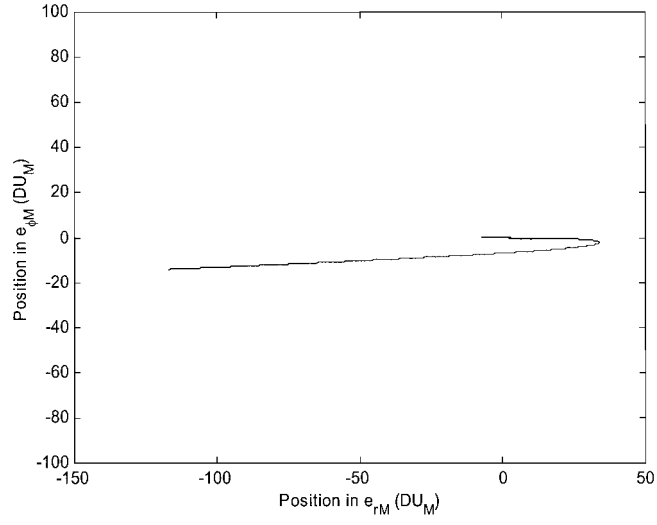

Fig. 3c Out-of-plane projection of 9-day capture segment of 145-day trajectory.

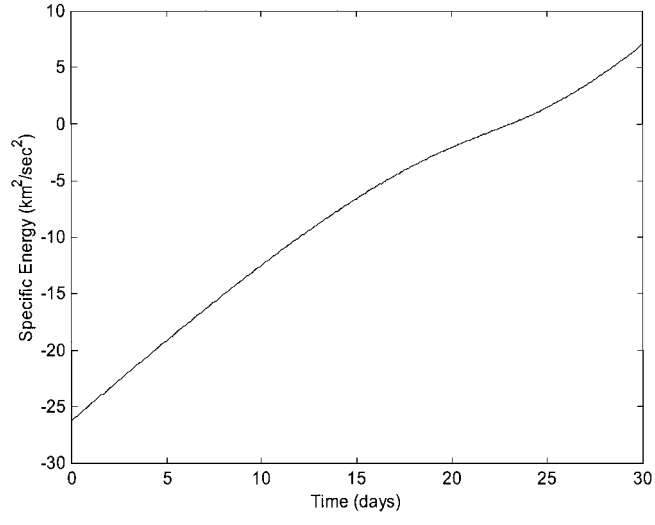

Fig. 3d Specific energy relative to Earth for 30-day escape phase of 145-day trajectory.

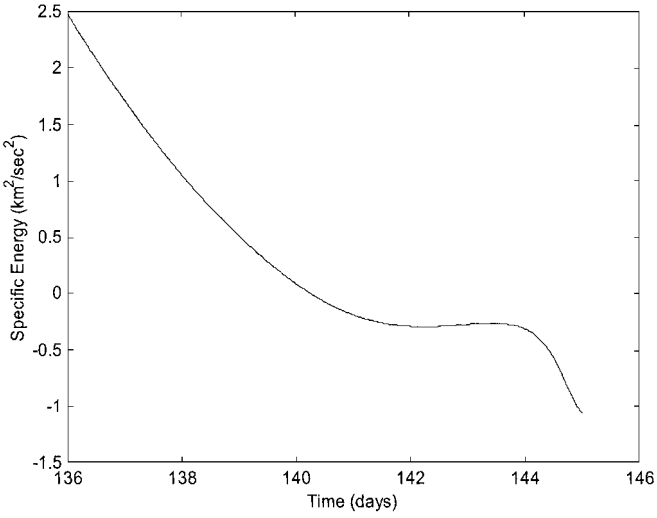

Fig. 3e Specific energy with respect to Mars for 9-day capture phase of 145-day trajectory.

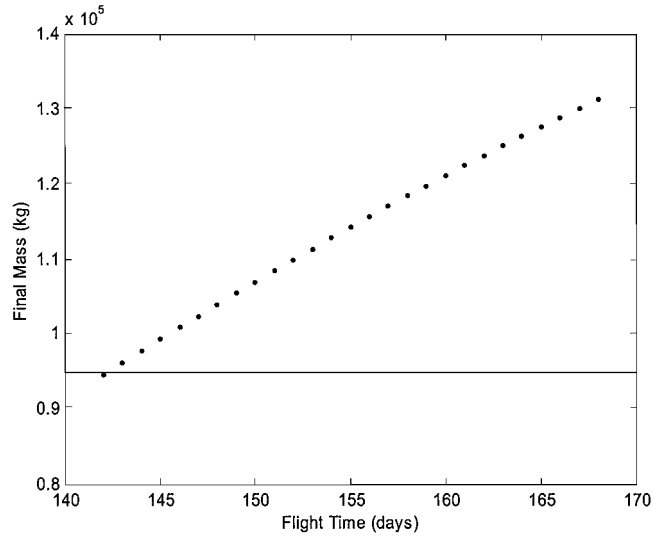

Fig. 4 Final mass vs flight time.

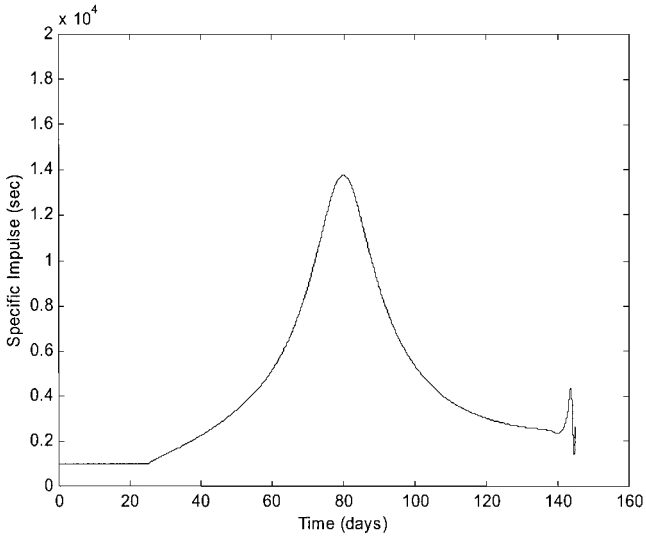

Fig. 3f I_{sp} variation for 145-day trajectory.

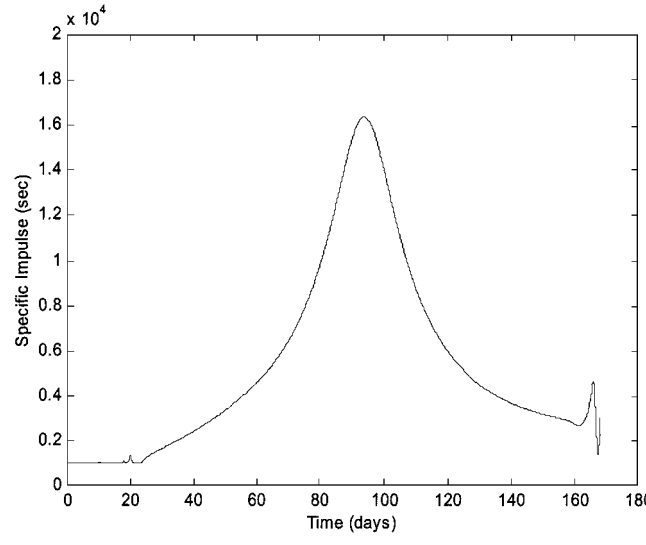

Fig. 5 I_{sp} variation for 168-day trajectory.

spacecraft reaches a near-coasting phase in the middle of the trajectory to trim down the fuel expenditure. The resulting final mass for this particular case is 99,316 kg, and an excess of 4316 kg of propellant remains at arrival.

The effect of the mission duration on the final spacecraft mass is depicted in Fig. 4 for trip times in the range of 142–168 days. As expected, the results show that a more fuel-efficient trajectory can be obtained with a relaxed mission time frame, within the limits considered. Figure 4 thus summarizes the tradeoff between trip time and fuel requirement. Note that the resulting final mass corresponding to the 142 day trajectory falls below the limit of 95,000 kg, rendering it infeasible.

The final mass obtained using the 168-day trajectory is 128,956 kg. Thus, an additional amount of 29,640 kg of excess fuel remains over that for the 145-day trajectory. The I_{sp} variation for the 168-day trajectory is plotted in Fig. 5. The plot is similar to that in Fig. 3f, except for the thrust modulations before escape as indicated by the spikes in the I_{sp} variation. This phenomenon has also been observed for planar trajectories shown in Ref. 12. Thus, thrust modulations can occur before escaping the Earth when the mission time frame is sufficiently relaxed, resulting in reduced fuel consumption.

With the trip time fixed at 145 days, power level set at 10 MW, and both i_0 and i_f specified at 0 deg, the effect on the final spacecraft mass due to a reduction in the initial mass was investigated. The initial mass was varied from the original 525,000 kg down to 420,000 kg. The variation of the final mass relative to the initial mass is plotted in Fig. 6. From these results, it is surmised that a more optimal trajectory can be achieved for this example if the initial mass of the spacecraft is approximately 480,000 kg. Moreover, there exist feasible solutions for values of the initial spacecraft mass below 420,000 kg. However, due to convergence difficulties, further reduction in the initial mass was not attainable.

In addition to the trajectory analysis with respect to the initial mass, the 145-day trajectory was also studied as a function of the available power level. With the initial mass fixed at 525,000 kg and both arrival and departure inclinations set at 0 deg, trajectories with power levels lower than 10 MW were determined. Again, due to convergence difficulties, only trajectories with power levels as low as 9.3 MW could be computed. The effect on the final mass due to the power reduction is shown in Fig. 7. The solid line in the Fig. 7 is a plot of the final mass constraint based on the 6-kg/kW specific mass of the power plant. The plot shows that lower power results in a decrease in the final mass, which is not a surprising result.

Example Set 2

In this set of examples, the final conditions were enforced for capture at nonzero i_f. Trajectories with a trip time of 145 days were determined for various i_f values from 0 to 88 deg. The trajectories were computed with all of the other parameters fixed at their nominal values, for example, initial mass of 525,000 kg and power level of 10 MW. The effect on the final mass due to variation of i_f is

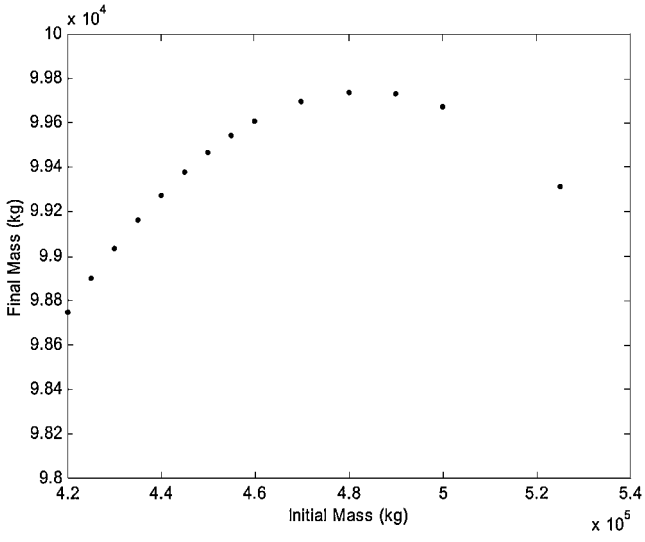

Fig. 6 Final mass vs initial mass.

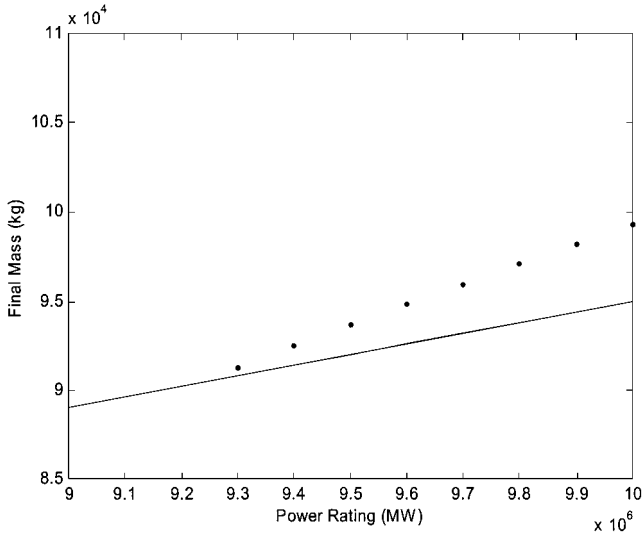

Fig. 7 Final mass vs power level.

presented in Fig. 8. The plot reveals that, for the departure date considered, higher efficiency is achieved by establishing a near-polar orbit about Mars.

The in-plane and out-of-plane projections of the 7-day capture phase, during which the spacecraft establishes an 88-deg inclined orbit about Mars, are shown in Figs. 9a and 9b, respectively. The path toward circularization is considerably smoother in this case compared to that with capture at an inclination of 0 deg. The final mass associated with this trajectory is 103,574 kg. This trajectory requires 4258 kg less fuel than that with circularization at an inclination of 0 deg. The enhanced fuel efficiency in this case is due to the smoother terminal maneuver as compared to that with $i_f = 0$ deg.

With the nominal initial mass and power level, and with $i_f =$ 88 deg, alternative initial conditions were applied to obtain 145-day trajectories departing at nonzero i_0 values. The resulting final spacecraft masses corresponding to trajectories with departure inclinations up to $i_0 = 30$ deg showed variations of the order of 5 kg only. The inclination relative to the Earth's equator, associated with each i_0 between 0 and 30 deg, were calculated based on the resulting values of $\theta_1(t_0)$ and $\phi_1(t_0)$. It was seen that the trajectories with i_0 greater than approximately 11.5 deg resulted in equatorial inclinations above 28.5 deg. Hence, the required parking orbits for the trajectories with i_0 greater than approximately 11.5 deg can be achieved without predeparture plane changes, assuming launches from Cape Canaveral, Florida, at a latitude of 28.5°.

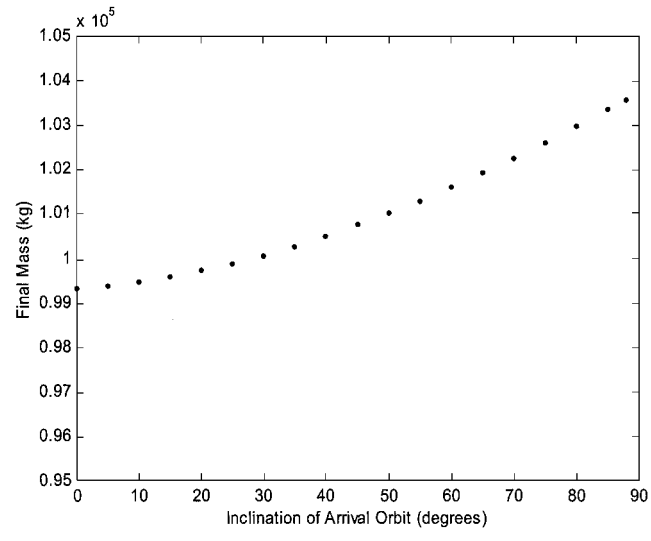

Fig. 8 Final mass vs arrival orbit inclination.

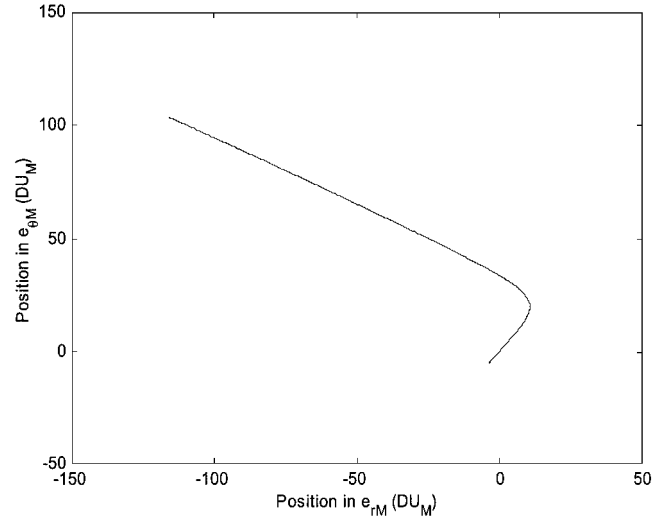

Fig. 9a In-plane projection of 7-day capture segment of 145-day trajectory with i_f = 88 deg.

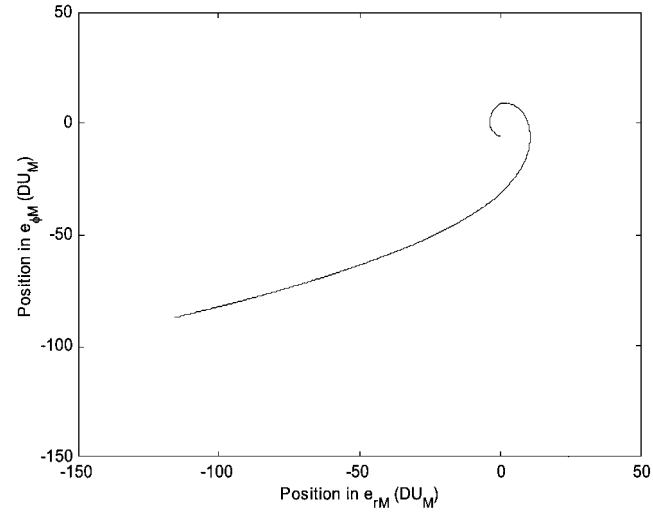

Fig. 9b Out-of-plane projection of 7-day capture segment of 145-day trajectory with i_f = 88 deg.

Conclusions

Fuel-optimal, three-dimensional rocket trajectories utilizing the characteristics of a variable specific impulse I_{sp} plasma thruster are presented and analyzed. Gravitational effects of the sun, Earth, and Mars were included in the computations. The optimal control problems were solved using an indirect multiple-shooting method. For the range of final times considered, it is seen that higher fuel efficiency can be achieved with a longer trip time. It is observed that during the Earth-escape phase, I_{sp} modulations result if the trip time is sufficiently relaxed. For the departure date considered in this work, trajectories with near-polar inclinations relative to the orbital plane of Mars seem to be more fuel optimal. Inclination of the departure trajectory, however, shows an insignificant effect on the final mass. From the trend of the final mass variation due to initial mass reduction, trajectories with initial masses lower than 420,000 kg at departure are feasible. They were simply not computable due to numerical sensitivity with the method applied in this work. The investigation on the effect of reducing the power level concludes that a lower final mass will result with lower power rating. Both trip time and power levels are tradeoff factors that have significant influence on the final spacecraft mass.

Acknowledgments

We thank Hans Seywald of Analytical Mechanics Associates for supplying the software used for numerical computations in this work. Suggestions and feedback from B. Cockrell of NASA Johnson Space Center are greatly appreciated.

References

[1]Chang-Diaz, F. R., Hsu, M. M., Braden, E., Johnson, I., and Yang, T. F., "Rapid Mars Transits with Exhaust-Modulated Plasma Propulsion," NASA TP 3539, March 1995.

[2]Melbourne, W. G., "Interplanetary and Payload Capability of Advanced Propulsion Vehicle," Jet Propulsion Lab. TR 32-68, California Inst. of Technology, Pasadena, CA, March 1961.

[3]Sheppard, J., Broome, J., Johnson, I., and Braden, E., "Power-Limited Human Mission to Mars," NASA Johnson Space Center, JSC 28436, Sept. 1998.

[4]Kechichian, J. A., "Optimal Low-Thrust Orbit Transfer," *Orbital Mechanics,* edited by V. A. Chobotov, 2nd ed., AIAA, Reston, VA, 1996, pp. 327–402.

[5]Kluever, C. A., "Optimal Low-Thrust Interplanetary Trajectories by Direct Method Techniques," *Journal of Astronautical Sciences,* Vol. 45, No. 3, 1997, pp. 247–262.

[6]Coverstone-Carroll, V., and Williams, S. N., "Optimal Low Thrust Trajectories Using Differential Inclusion Concepts," *Journal of Astronautical Sciences,* Vol. 42, No. 4, 1994, pp. 379–393.

[7]Enright, P. J., and Conway, B. A., "Discrete Approximations to Optimal Trajectories Using Direct Transcription and Nonlinear Programming," *Journal of Guidance, Control, and Dynamics,* Vol. 15, No. 4, 1992, pp. 994–1002.

[8]Scheel, W. A., and Conway, B. A., "Optimization of Very-Low-Thrust, Many Revolution Spacecraft Trajectories," *Journal of Guidance, Control, and Dynamics,* Vol. 17, No. 6, 1994, pp. 1185–1192.

[9]Pierson, B. L., and Kluever, C. A., "Three-Stage Approach to Optimal Low-Thrust Earth–Moon Trajectories," *Journal of Guidance, Control, and Dynamics,* Vol. 17, No. 6, 1994, pp. 1275–1282.

[10]Kluever, C. A., and Pierson, B. L., "Optimal Low-Thrust Three-Dimensional Earth–Moon Trajectories," *Journal of Guidance, Control, and Dynamics,* Vol. 18, No. 4, 1995, pp. 830–837.

[11]Tang, S., and Conway, B. A., "Optimization of Low-Thrust Interplanetary Trajectories Using Collocation and Nonlinear Programming," *Journal of Guidance, Control, and Dynamics,* Vol. 18, No. 3, 1995, pp. 599–604.

[12]Vadali, S. R., Nah, R., Braden, E., and Johnson, I. L., "Fuel-Optimal Planar Interplanetary Trajectories Using Low-Thrust Exhaust-Modulated Propulsion," AAS Paper 99-132, Feb. 1999; also *Journal of Guidance, Control, and Dynamics*, Vol. 23, No. 3, 2000, pp. 476–482.

[13]Nah, R. S., "Fuel-Optimal Earth–Mars Trajectories Using Low-Thrust Exhaust-Modulated Plasma Propulsion," M.S. Thesis, Dept. of Aerospace Engineering, Texas A&M Univ., College Station, TX, Dec. 1999.

[14]Lewis, F. L., and Syrmos, V. L., *Optimal Control,* 2nd ed., Wiley, New York, 1995, pp. 129–203, 259–311.

[15]Bate, R. R., Mueller, D. D., and White, J. E., *Fundamentals of Astrodynamics,* Dover, New York, 1971, p. 429.